1990

Principles and Clinical Applications of Magnetic Resonance

Rao P. Gullapalli
University of Arkansas at Little Rock

Teresa T. Evans
University of Arkansas at Little Rock

Roger M. Hawk
University of Arkansas at Little Rock

Follow this and additional works at: http://scholarworks.uark.edu/jaas

Part of the Electromagnetics and Photonics Commons, and the Nuclear Commons

PRINCIPLES AND CLINICAL APPLICATIONS OF MAGNETIC RESONANCE

RAO P. GULLAPALLI[1], TERESA T. EVANS[2], and ROGER M. HAWK[1]
University of Arkansas at Little Rock
[1]Department of Electronics and Instrumentation
[2]Department of Chemistry
2801 S. University
Little Rock, AR 72204

ABSTRACT

A review is presented which covers the basic theory of nuclear magnetic resonance (NMR) with regard to angular momentum, magnetic moments, and the classical mechanical description of the NMR experiment. Longitudinal (T_1) and Transverse (T_2) relaxation times are defined as well as the basic pulse sequences used for their measurement. In particular, the $180°$-τ-$90°$ and the Hahn Spin Echo pulse sequences are described in detail. Basic Magnetic Resonance Imaging (MRI) theory is discussed with regard to slice selection, frequency encoding, and phase encoding to define the imaged volume element. The equations defining the amount of T_1, T_2, and proton density which contribute to the images are discussed. Common MRI pulsing sequences are described in detail as well as the imaging time equation. Recent in-vivo magnetic resonance studies involving the use of contrast agents, and the use of localized spectroscopy, specifically ^{13}C, ^{19}F, ^{23}Na and ^{39}K, are discussed.

INTRODUCTION

Nuclear magnetic resonance (NMR) imaging of the human body is a relatively new diagnostic technique. It normally is referred to as magnetic resonance imaging or MRI. Figure 1 shows a general block
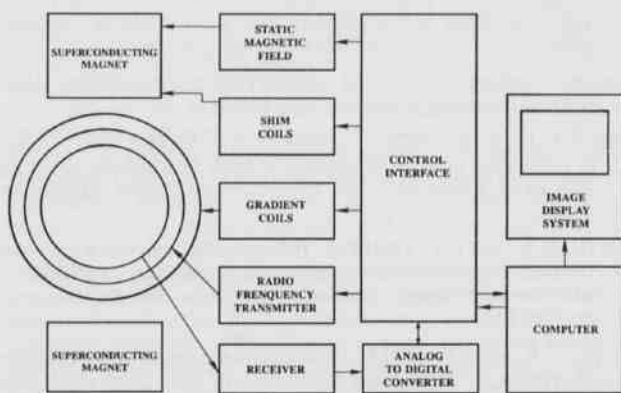

Figure 1. Schematic of a Typical Magnetic Imaging Spectrometer.

diagram for an MRI system. The patient is placed in a strong magnetic field and radio frequency (RF) pulses are controlled to irradiate a specific volume in MRI. Intensity-modulated images are generated for the body by use of these RF and magnetic fields. Three separate magnetic fields are used. These are the main magnetic field (or the Zeeman field), gradient magnetic fields (G_z, G_x, G_y), and the RF field (or electromagnetic field). The main magnetic field also is known as the static field, $\overline{B}_0$. It is used to align the atomic nuclei and is maintained constant throughout the imaging procedure. The main field strength is typically 1,000 to 15,000 gauss or 0.1 to 1.5 Tesla. The imaged voxel or volume element is defined by the gradient magnetic fields. During the imaging sequence, the gradient fields are rapidly switched for the spatial localization of the resonance. The third electromagnetic field, the RF field,

is used to excite the atomic nuclei at their characteristic resonance frequency given by the Larmor equation. The average power of an RF pulse that irradiates the patient is 50 to 500 watts with a duration of between 1 and 10 milliseconds.

In an image, the determination of signal intensities at specific locations is dependent upon proton density and the tissue's chemical environment. The nuclear response from the patient is detected, which upon Fourier transformation and software manipulation is converted into a contrasted image. By using the knowledge of the chemical structure of certain parts of the body, different imaging techniques can be used that change the appearance of the image dramatically. MRI also can be used for in-vivo body chemistry measurements as well as giving anatomical high-quality images.

BASIC THEORY

ANGULAR MOMENTUM

Certain nuclei containing an odd number of protons, when placed in a magnetic field, behave as if they were spinning charged particles. Nuclei that possess this property have associated angular momenta, $\overline{P}$. The maximum observable component of angular momentum is:

$$\overline{P} = \frac{h}{2\pi} \overline{I} = \hbar \overline{I} \qquad (1)$$

where $\overline{I}$ equals the dimensionless angular momentum vector operator and h is Planck's constant.

Nuclei can be classified by their nuclear spin which is also called the nuclear spin quantum number I. Some nuclei, however, possess no angular momenta when their I equals zero. These nuclei with even atomic numbers and even mass numbers (for example, ^{12}C, ^{16}O, and ^{32}S) cannot experience magnetic resonance under any circumstance.

MAGNETIC MOMENT

Each nucleus with $I \neq 0$ possesses a magnetic dipole moment or a magnetic moment, $\overline{\mu}$, which is expressed as:

Rao P. Gullapalli, Teresa T. Evans, and Roger M. Hawk

$$\bar{\mu} = \gamma \, \bar{P} \qquad (2)$$

where γ is called the magnetogyric ratio or gyromagnetic ratio; γ is different for different nuclei and is given by:

$$\gamma = \frac{q}{2 \, mc} \qquad (3)$$

where q is the charge of the nucleus in electrostatic units, m is the mass of the nucleus in grams, and c equals the speed of light in cm sec^{-1}.

The gyromagnetic ratio accounts for nuclear properties not accounted for by the simple picture of a spinning charged particle. $\bar{P}$ is a simple multiple of h as shown in equation (1), but $\bar{\mu}$ and γ are not, and both $\bar{\mu}$ and γ must be determined experimentally for each nucleus. Table 1 lists nuclei of medical interest and their associated gyromagnetic ratios.

Table 1. Nuclear Spin Properties for Some Common Nuclei.

ISOTOPE	I	NMR FREQUENCY IN A 2.3487 TESLA FIELD (MHz.)	NATURAL ABUNDANCE %	RELATIVE SENSITIVITY AT CONSTANT FIELD
^{1}H	1/2	100.00	99.985	1.00
^{2}H	1	15.35	0.015	0.00000145
^{7}Li	3/2	38.86	92.58	0.27123
^{11}B	3/2	32.08	80.42	0.133
^{13}C	1/2	25.14	1.1	0.00018
^{14}N	1	7.22	99.63	0.001
^{15}N	-1/2	10.13	0.37	0.000004
^{17}O	-5/2	13.56	0.037	0.00001
^{19}F	1/2	94.08	100.00	0.833
^{23}Na	3/2	26.45	100.00	0.0925
^{27}Al	5/2	26.06	100.00	0.206
^{29}Si	-1/2	19.86	4.70	0.0037
^{31}P	1/2	40.48	100.00	0.066
^{35}Cl	3/2	9.79	75.53	0.0035
^{119}Sn	-1/2	37.27	7.61	0.0044
^{195}Pt	1/2	21.50	33.80	0.0034
^{199}Hg	1/2	17.83	16.84	0.00019
^{207}Pb	1/2	20.92	22.6	0.002

CLASSICAL MECHANICAL DESCRIPTION OF NMR

Consider the interaction of a magnetic moment, $\bar{\mu}$, with an applied highly homogeneous magnetic field, $\bar{B}_o$, as shown in Fig. 2.

The magnetic interaction between $\bar{B}_o$ and $\bar{\mu}$ generates a torque tending to align $\bar{\mu}$ with $\bar{B}_o$. The magnetic moment, $\bar{\mu}$, does not align with $\bar{B}_o$, but instead $\bar{\mu}$ precesses around $\bar{B}_o$ at an angle Θ. This can be

Figure 2. Precession of a Magnetic Moment in a Steady Magnetic Field.

likened to a gyroscope which precesses around the earth's gravitational lines of force.

The precessional frequency for nuclei (with $I \neq O$) is given by the Larmor expression:

$$\bar{\omega}_L \text{ (radians sec}^{-1}) = -\gamma \, \bar{B}_o. \qquad (4)$$

Thus, the magnetic moment precesses around $\bar{B}_o$ at the Larmor frequency:

$$\gamma_L \text{ (Hertz)} = \frac{|\bar{\omega}_L|}{2\pi} = \frac{\gamma \, |\bar{B}_o|}{2\pi}. \qquad (5)$$

Notice that the angle Θ does not appear and, hence, the nucleus will precess at a frequency governed by its own characteristic gyromagnetic ratio and the magnitude of the magnetic field. Energy, however, is dependent on the angle since classically:

$$E = -\bar{\mu} \cdot \bar{B}_o = -\mu \, B_o \cos \Theta. \qquad (6)$$

We never study a single nuclear amount, $\bar{\mu}$, but rather an ensemble containing a large number of magnetic moments as shown in Fig. 3.
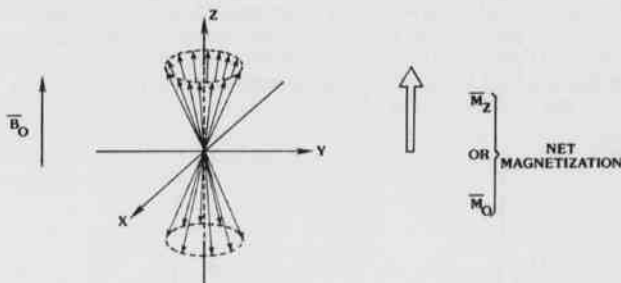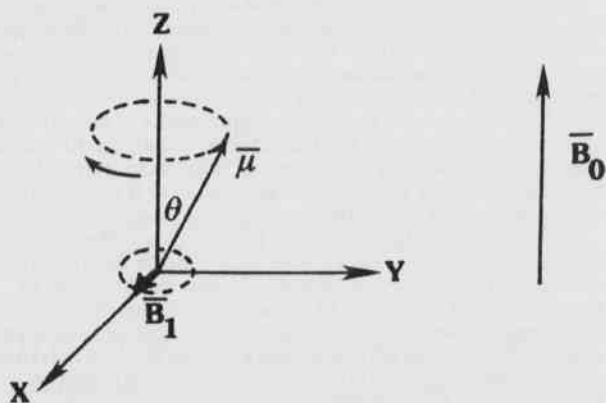
Figure 3. Vector Addition of Magnetic Moments to Form the Macroscopic Magnetization or Net Magnetization for an Ensemble of Identical Magnetic Moments of Nuclei with $I = 1/2$.

The individual magnetic moments precess around the magnetic field in $2I + 1$ possible energy states (Emsley *et al.*, 1965). Thus, for a nucleus with spin 1/2, (for example ^{1}H, ^{13}C, ^{19}F, and ^{31}P) there are two possible energy states. All moments precess at the same frequency, but without phase coherence in the x-y plane. There is a net magnetization $\bar{M}_z$ or $\bar{M}_o$ along the z axis defined by the presence of the magnetic field $\bar{B}_o$, since the Boltzmann distribution slightly favors the lower energy state, that is, aligned along the direction of $\bar{B}_o$.

For nuclei of spin I, the net magnetization is given by (Pake, 1950):

$$\bar{M}_o = \frac{N \gamma^2 \hbar^2 I (I + 1)}{3 \, k \, T} \bar{B}_o, \qquad (7)$$

where k = Boltzmann constant and T = temperature (K).

RF PULSES

In nuclear magnetic resonance experiments, the response of a sample's nuclear magnetization to a time varying external magnetic field $\bar{B}(t) = \bar{B}_o + \bar{B}_1(t)$ is usually investigated. During application of $\bar{B}_1(t)$ at the Larmor frequency, $\bar{B}_o$ becomes vanishingly small and, therefore, the net magnetization $\bar{M}_o$ begins to precess around the direction of the applied RF field, $\bar{B}_1(t)$ (Hahn, 1950). Energy is absorbed from the field $\bar{B}_1(t)$ only when:

57

Principles and Clinical Applications of Magnetic Resonance

$$\gamma_{\bar{B}_1(t)} = \gamma_L. \qquad (8)$$

The magnetic vector of the $\bar{B}_1(t)$ field can be thought of as rotating in the x-y plane as shown in Fig. 2. In practice, the rotating field $B_1(t)$ is obtained from a linearly polarized electromagnetic field that results from the passage of electric current at frequency γ through the transmitter coil.

On absorption of energy from $\bar{B}_1(t)$, each individual magnetic moment tips to a different angle Θ, but their precessional frequency remains constant as expressed by the Larmor relation (Slichter, 1963).

In a time t_p(sec), the angle through which $\bar{M}_o$ rotates is given by:

$$\Theta(\text{radians}) = \gamma |\bar{B}_1(t)| t_p \qquad (10)$$

Consequently, by controlling the time of the applied RF $\bar{B}_1(t)$ pulse, $\bar{M}_o$ can be rotated clockwise through any angle Θ.

Two RF pulse lengths are used most often in MRI. These are referred to as 90° ($\pi/2$) and 180° (π) pulses (Farrar and Becker, 1971). The equations which describe the behavior of nuclear spin in relation to a fixed coordinate system are very complex. Substantial simplification is achieved if nuclear spin motions are referred to a coordinate system which rotates about the direction of the fixed $\bar{B}_o$ magnetic field with a frequency equal to the frequency of the applied RF field. The coordinate axes in this rotating frame are designated by the use of primes. A pictorial description of the reorientation of $\bar{M}_o$ before and after application of $\bar{B}_1(t)$ for a duration t_p to reorientate $\bar{M}_o$ on either the y' or -z' axis is shown in Fig. 4.
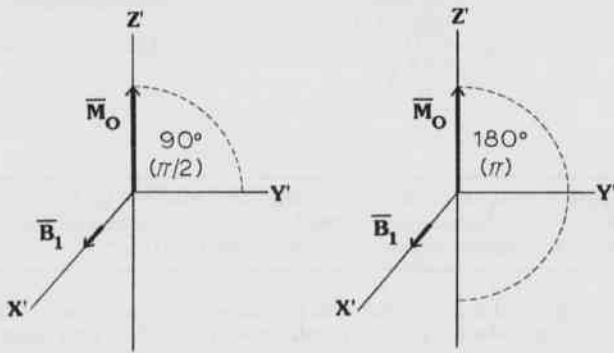

Figure 4. Precession of $\bar{M}_o$ about $\bar{B}_1$ in the Rotating Frame by $\pi/2$ or π radians.

After a pulsed RF field $\bar{B}_1(t)$, an ensemble of N equal spins will relax toward the equilibrium magnetization, given previously by equation 7. Normally, relaxation is described in terms of the time evolution of the parallel and perpendicular components of an instantaneous magnetization $\bar{M}(t)$ (with respect to the Zeeman field $\bar{B}_o$) after $\bar{B}_1(t)$ is removed; time constants, T_1 and T_2, are associated with these parallel and perpendicular components of $\bar{M}(t)$ (Abragam, 1961). In practice, high power RF pulses are used such that $t_p << T_1, T_2$ and, therefore, no significant relaxation occurs during the RF pulses.

DEFINITION OF THE LONGITUDINAL (T_1) AND TRANSVERSE (T_2) RELAXATION TIMES

In an NMR experiment, an RF field $\bar{B}_1(t)$ ($\bar{B}_1(t) << \bar{B}_o$) is applied at the Larmor frequency at right angles to $\bar{B}_o$ as was shown in Figure 2. Application of $\bar{B}_1(t)$ causes spin transitions from the lower to the higher energy state thereby causing the original Boltzmann equilibrium

population difference between the lower and upper spin states (Fig. 5a) to decrease. Also, $\bar{B}_1(t)$ causes the individual spins to precess in phase thereby generating a net $\bar{M}_{x,y}$ component of spin in the x-y plane as shown in Figs. 5b and c.
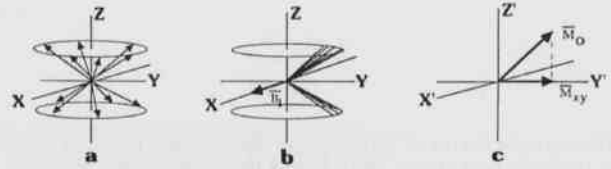

Figure 5. Phase Coherence and Movement of Magnetization Toward the x-y Plane: (a) Nuclei Precessing at Equilibrium, (b) Coherence of Vectors due to Application of $\bar{B}_1$, (c) Net Magnetization and Component in the x-y Plane after Application of $\bar{B}_1$.

After $\bar{B}_1(t)$ is turned off, the imposed phase coherence of the spins immediately begins to decrease due to the presence of local magnetic fields at each nuclear site which add to or subtract from $\bar{B}_o$. Therefore, the spins have a range of precessional frequencies which cause the loss of phase coherence and, thus, any $\bar{M}_{x,y}$ component of spin. Simultaneous spin flips involving two antiparallel spins also can lead to loss of phase coherence. The time scale for loss of the $\bar{M}_{x,y}$ component of spin is associated with a transverse or spin-spin relaxation time constant, T_2.

Reestablishment of the original thermal equilibrium between the spins and the surroundings or the "lattice" also occurs while phase coherence is being lost, and this energy dissipating process is described by a spin-lattice or longitudinal relaxation time constant, T_1. At thermal equilibrium, the spin ensemble has random phase with no $\bar{M}_{x,y}$ component of magnetization; therefore T_1 must by necessity satisfy the condition $T_1 \geq T_2$ (Hawk, 1973).

FREE INDUCTION DECAY

Suppose a 90° pulse is applied along the x' axis in the frame rotating at the RF frequency. Following the pulse, $\bar{M}_{x,y}$ lies entirely along the y' axis, as indicated in Fig. 5c. Since the probe assembly is arranged to detect signals induced in a receiver coil along the fixed x or y axis, the magnitude of $\bar{M}_{x,y}$ determines the strength of the observed signal (called a free induction decay [FID] signal). As transverse relaxation occurs, the signal decays. In a perfectly homogeneous field, the time constant of the decay would be T_2, however, the free induction decay signal actually decays in a time T_2^* that is determined primarily by B_o inhomogeneity. This is a consequence of the fact that nuclei in different parts of the field precess at slightly different frequencies, and therefore, phase coherence is lost.

Figure 6a shows the pure exponential decay that results from an RF pulse applied exactly at the resonance frequency of a single type of nucleus. This decay directly measures the decrease in $\bar{M}_{x,y}$ since the usual experimental arrangement provides a detector which is phase referenced to the RF transmitter (Farrar and Becker, 1971). Thus, even though detection of the signal occurs when no RF is directly applied to the nuclear spin system (that is, after the pulse), the RF reference is applied to the detector continuously. The detector responds to the magnetization which has a fixed phase relation to $\bar{B}_1(t)$, which occurs along a fixed axis in the rotating frame (in this case the positive y' axis).

Suppose now that the transmitter RF is slightly different from the Larmor frequency of the nuclei. If we again consider the frame rotating at the radio frequency, then immediately after the 90° pulse, $\bar{M}_{x,y}$ lies along the y' axis. However, $\bar{M}_{x,y}$ now rotates relative to the rotating frame, and the detector displays not only the exponentially decaying value of $\bar{M}_{x,y}$, but also the interference effects as $\bar{M}_{x,y}$ and the reference frequency alternately come in and out of phase with each other. A typical FID response is shown in Fig. 6b.

Measurement of the free induction decay is how the magnitude and other characteristics of $\bar{M}_o$ are determined. The four components of an FID are shown in Fig. 7. The FID following a 90° pulse provides

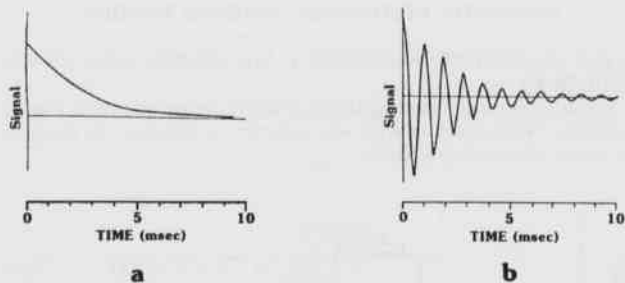### Rao P. Gullapalli, Teresa T. Evans, and Roger M. Hawk

Figure 6. (a) Free Induction Decay (FID) for RF Precisely at the Larmor Frequency (b) FID for RF off Resonance.
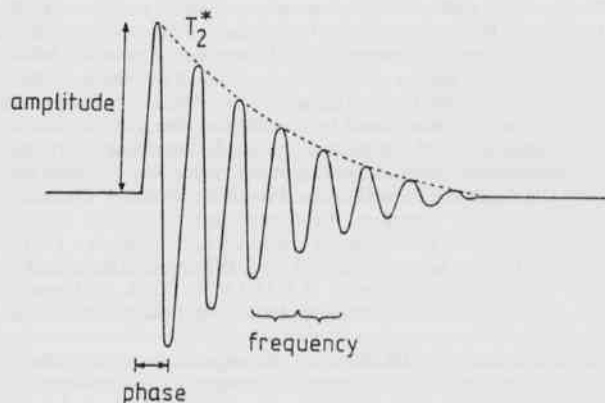

Figure 7. The Informational Content of an FID.

the spectral information required in Fourier transform NMR, and the FID resulting from sequences of two or more pulses is used in the determination of T_1 and T_2 relaxation times. Proton density (ρ) is determined from the initial amplitude which is proportional to the number of hydrogen nuclei.

In Fig. 8, $\overline{M}_z$ and $\overline{M}_{x,y}$ are plotted as a function of time. The equations for the two curves are:

$$\overline{M}_z = \overline{M}_0 [1 - e^{-t/T_1}] \tag{11}$$

$$\overline{M}_{x,y} = \overline{M}_0 e^{-t/T_1} . \tag{12}$$

MRI images of tissues are generated from the T_1, T_2, and hydrogen nuclei density measurements. The chemical structure determines the contrast.

RELAXATION TIME CONSTANT MEASUREMENTS

180°-τ-90° SEQUENCE FOR THE MEASUREMENT OF T_1

The longitudinal relaxation time, T_1, is often measured by the 180°-τ-90° sequence where an initial 180° pulse directed along the x' axis rotates the equilibrium magnetization clockwise from the +z' to
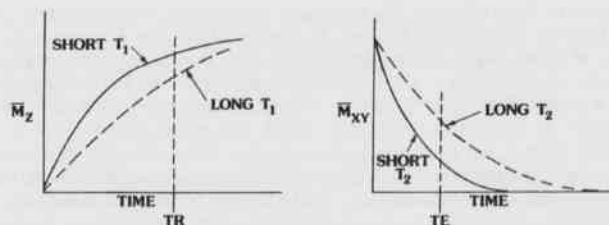

Figure 8. Recovery for $\overline{M}_z$ with Short and Long T_1 Values and Loss of Phase Coherence ($\overline{M}_{xy}$) in the x-y Plane for Short and Long T_2 Values.

the −x' axis. After a variable time τ, during which nuclear relaxation occurs, a 90° pulse directed along the x' axis rotates the magnetization clockwise 90°. Whether the magnetization is rotated to the +y' or the −y' axis depends on the time interval τ relative to the value of T_1. If τ << T_1, the magnetization which was rotated to the −z' axis by the first 180° pulse will have just begun its exponential recovery toward reestablishment of the equilibrium magnetization. Therefore, the magnetization will lie along the −z' axis and the 90° pulse will rotate this magnetization clockwise to the −y' axis. The signal is nulled when the time interval τ = .69T_1 since the magnetization passes through the origin.

If τ > .69T_1, the magnetization will lie along the +z' axis and the 90° pulse will align the magnetization along the +y' direction. Thus, a plot of the sampled magnetization versus τ will yield the exponential plot shown in Fig. 9; each dot corresponds to a separate 180°-τ-90° sequence.
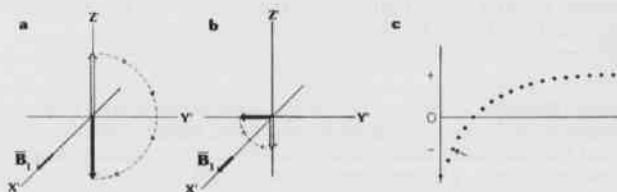

Figure 9. Determination of T_1 by the 180°-τ-90° Sequence. (a) $\overline{M}_0$ inverted at time 0 by a π pulse, (b) $\overline{M}$ rotated by a π/2 pulse after a time τ, (c) The initial amplitude of the free induction decay is plotted as a function of τ. Each point corresponds to a separate 180°-τ-90° sequence. The point corresponding to (b) is indicated by the arrow.

A decided drawback of the 180°-τ-90° sequence is its relative inefficiency since a full 5T_1 time interval should be allowed to reestablish the equilibrium magnetization before initiation of the next sampling sequence. Also, only one point is measured on the exponential curve for each 180°-τ-90° pulse sequence (Hawk, 1973).

MEASUREMENT OF T_2 BY THE SPIN-ECHO METHOD

The contribution of inhomogeneity in $\overline{B}_0$ precludes the use of the decay time, T_2^*, as a measure of T_2. An ingenious method for overcoming the inhomogeneity problem was first proposed by Hahn (1950), who called it the spin-echo method. The method consists of the application of a 90°-τ-180° sequence and the observation at a time 2τ of a free induction "echo" (Farrar and Becker, 1971). The method is shown in Fig. 10 which depicts the behavior of the magnetization in the rotating

Principles and Clinical Applications of Magnetic Resonance

frame. In Figure 10 (a), $\overline{M}_o$ is rotated through 90° by application of $\overline{B}_1(t)$ along the positive x′ axis. In Figure 10 (b), the $\overline{\mu}_i$ begin to fan out, as some nuclei precess faster and some slower than the rotating frame which rotates at the reference frequency of the RF transmitter. At a time τ after the 90° pulse, a 180° pulse is applied, also along the positive x′ axis, as shown in Fig. 10 (c). The effect of this pulse is to rotate each $\overline{\mu}_i$ by 180° about the x′ axis. Thus, those $\overline{\mu}_i$ that were moving faster than the frame (shown in [b] moving toward the observer or clockwise looking down the z′ axis) naturally continue to move faster, but in Fig. 10 (d) their motion is now away from the observer. At time 2τ, all $\overline{\mu}_i$ come into phase along the negative y′ axis as shown in Figure 10 (e). The continuing movement of the $\overline{\mu}_i$ causes them again to lose phase coherence in Fig. 10 (f).
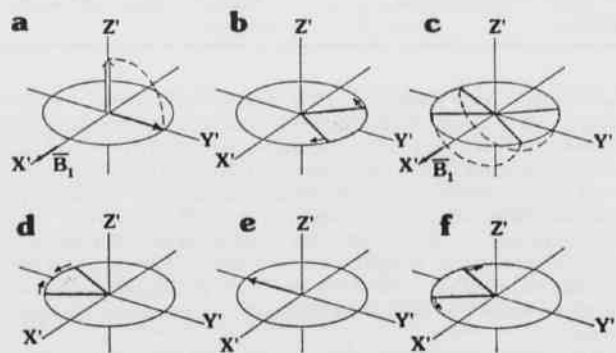

Figure 10. The Hahn Spin-Echo Experiment. (a) $\overline{M}_o$ is rotated through 90° by application of $\overline{B}_1$, (b) the $\overline{\mu}_i$ begins to fan out, (c) application of a 180° pulse at a time τ rotates all $\overline{\mu}_i$ about the x axis, (d) The $\overline{\mu}_i$ continue their relative motion with respect to the rotating frame frequency, (e) At a time 2τ all $\overline{\mu}_i$ refocus along the −y axis creating an echo, and (f) The $\overline{\mu}_i$ begin to dephase after the time 2τ.

The rephasing of the $\overline{\mu}_i$ causes a free induction signal to build to a maximum at 2τ, but the signal is, of course, negative relative to the initial free induction decay since rephasing of the $\overline{\mu}_i$ occurs along the negative y′ axis. If transverse relaxation did not occur, the echo amplitude would be as large as the initial value of the signal following the 90° pulse. However, each $\overline{\mu}_i$ decreases in magnitude during the time 2τ because of the natural processes responsible for transverse relaxation. Thus, the echo amplitude depends on T_2, and this quantity may in principle be determined from a plot of peak echo amplitude as a function of τ. As in the measurement of T_1, it is necessary to carry out a separate pulse sequence for each value of τ and to wait between pulse sequences as adequate time (at least five times T_1) for restoration of equilibrium. A typical set of data from a multiple spin-echo experiment is shown in Fig. 11.
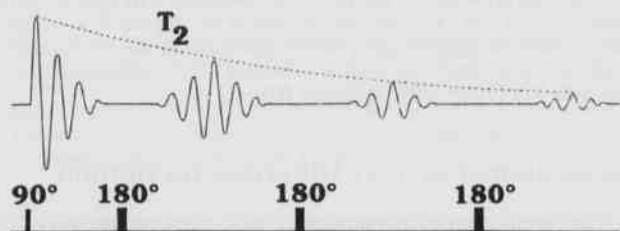

Figure 11. A Typical Carr-Purcell Experiment. Connection of the Peak Amplitudes of Each Successive Spin-Echo Defines the "True" T_2 Relaxation Time.

MAGNETIC RESONANCE IMAGING THEORY

SLICE SELECTION, FREQUENCY ENCODING, AND PHASE ENCODING

In transverse slice imaging, the coordinate system shown in Fig. 12 is chosen. The z direction is the slice selection, x direction the frequency, and y direction the phase.
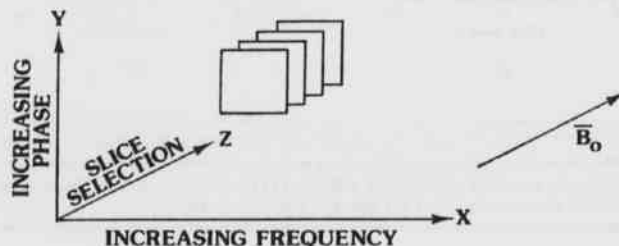

Figure 12. The Coordinate System for an MRI Experiment.

Firstly, the z gradient (G_z) is turned on to select the plane or slice to be imaged. When the z gradient is on, the field strength at one end of the magnet bore is stronger than at the other. Therefore, when a 90° pulse is turned on at a specific frequency, only protons in a specific slice (which satisfy the Larmor equation) are excited. The thickness of the selected slice is determined by the slope of the gradient field and the frequency width of the RF pulse which is controlled by the pulse power and pulse duration. According to RF theory, the frequency range spanned by a pulse of RF is equal to: Frequency Range = Transmitter Frequency ± $1/t_p$. Therefore, if the transmitter frequency were 42.6 MHz (corresponding to the Larmor frequency for protons in a 1.0 Tesla field) and if the t_p selected were 10 μsec, the actual transmitted frequency would cover the range of 42.5-42.7 MHz. Thus, the longer the pulse, the narrower the slice that can be selected since the RF frequency spread is reduced.

At the termination of the 90° pulse, all magnetic moments in the slice are precessing in phase at the same frequency and, thus, no spatial information can be obtained. Spatial locations can be obtained, however, by frequency and phase encoding of the precessing nuclei. Phase can be encoded in the y direction by turning off the slice-selection gradient, G_z, and turning on the phase-encoding gradient, G_y. While the phase-encoding gradient is on, the processional frequencies will increase linearly in the y direction in proportion to the applied gradient field strength. When this gradient is turned off, the precessional frequencies will be the same again; however, the phase angles will be different along the y direction (that is, the phase has been encoded). For readout, the slice-selection gradient (G_z) is again turned on, the 180° RF pulse is triggered, the slice-selection gradient is turned off, and the frequency-encoding gradient (G_x) is turned on during echo reception. The gradient in the x direction increases the frequencies of the received echoes linerally in the x direction so that spatial information can be obtained in the x direction (that is, the frequency is encoded). The received echo consists of a series of frequencies of specific amplitude and phase where frequency determines the x coordinate, phase determines the y coordinate, and amplitude determines the signal intensity. All information is retrieved from the echo by applying the Fourier transform. In practice, because of the high resonant frequencies associated with the technique, a single phase-encoding step is performed for each y coordinate. Typically 128, 192, or 256 phase encoding steps are used to obtain a single column in one slice. Thus, the Single Slice-Single Echo pulsing sequence shown in Fig. 13, would be repeated 128, 192, or 256 times although only two are shown. Frequency is typically encoded in 256 increments, yielding array sizes of 256 X 128, 256 X 192, or 256 X 256 pixels.

For imaging the sagittal plane, the x gradient would be used for plane selection, and for imaging the coronal plane the y gradient would be used. The frequency and phase would be encoded by the other two gradients.

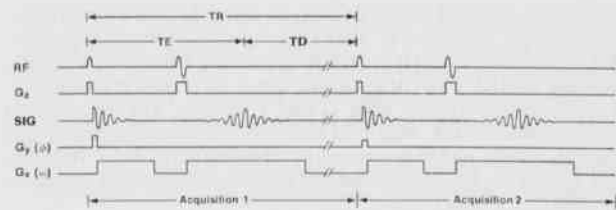Rao P. Gullapalli, Teresa T. Evans, and Roger M. Hawk

Figure 13. The Spin-Echo Sequence.

When the spin echo technique is used, the MRI signal intensity is given by:

$$SI = DF\,[1 - e^{-TD/T_1}]e^{-TE/T_2}$$

where D is a function of proton density and F is a flow factor (Bushong, 1988) and TD and TE are defined in Fig. 13.

In the data collection process, by defining TR, TE, and TD, the amount of T_1 and T_2 contributed to the images can be controlled. An example is where TE with respect to T_2 is shortened which reduces T_2 effects because e^{-TE/T_2} approaches 1. The T_1 effects can be reduced by making TD long with respect to T_1, because then e^{-TD/T_1} approaches 0. If both of these effects are reduced, then an image can be obtained that emphasizes the effects of proton density. To obtain an image that illustrates both T_2 and proton density, the T_2 contribution must be increased by lengthening TE while TD remains long. To increase the contribution of T_1 and obtain an image illustrating T_1 and proton density effects, TD would be shortened while TE remains short.

SINGLE SLICE-MULTIECHO METHOD

By increasing TE, the echo time, the T_2 effects are increased. Simultaneous echoes (which increase T_2 weighting) can be obtained by multiple echo times. The pulsing sequence for performing spin echo, single transverse-slice, multiecho imaging is shown in Figure 14. Each echo is diminished in amplitude as shown in Fig. 11. The TE increases with each additional 180° pulse, therefore, increasing the T_2 effects. The phase and frequency information is contained in each echo, which

is necessary for the generation of a single line for each image. The phase encoding and frequency encoding gradients are the same as those for the Single Slice-Single Echo sequence shown in Fig. 13.
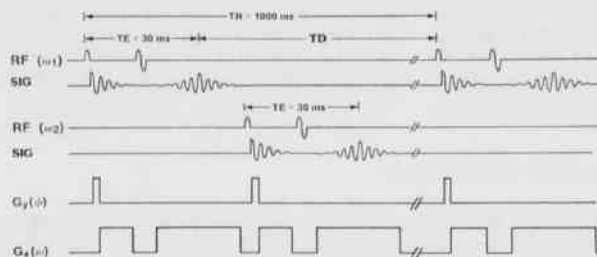

Figure 14. The RF Pulse Sequences Necessary for Multislice Spin Echo Imaging.

MULTISLICE-SINGLE ECHO

Another method is the multislice-single echo method shown in Fig. 14. In multislice imaging, TD, the recovery time, is used after the acquisition of the first slice to collect data from other slices. At each slice, one line at a time is used to collect data. The recovery time determines how many slices can be obtained. In order to prevent any overlap of adjacent slices, a small space is left between selected slices.

MULTISLICE-MULTIECHO

We can obtain multiple echo images from multiple slices by merging the multiecho sequence with the multislice sequence. The pulsing sequence for this multislice, multiecho imaging is shown in Fig. 15. Here, as in the a multislice-spin echo method, the recovery time from the first slice after the last echo is used to collect echoes from additional slices (Bushong, 1988).
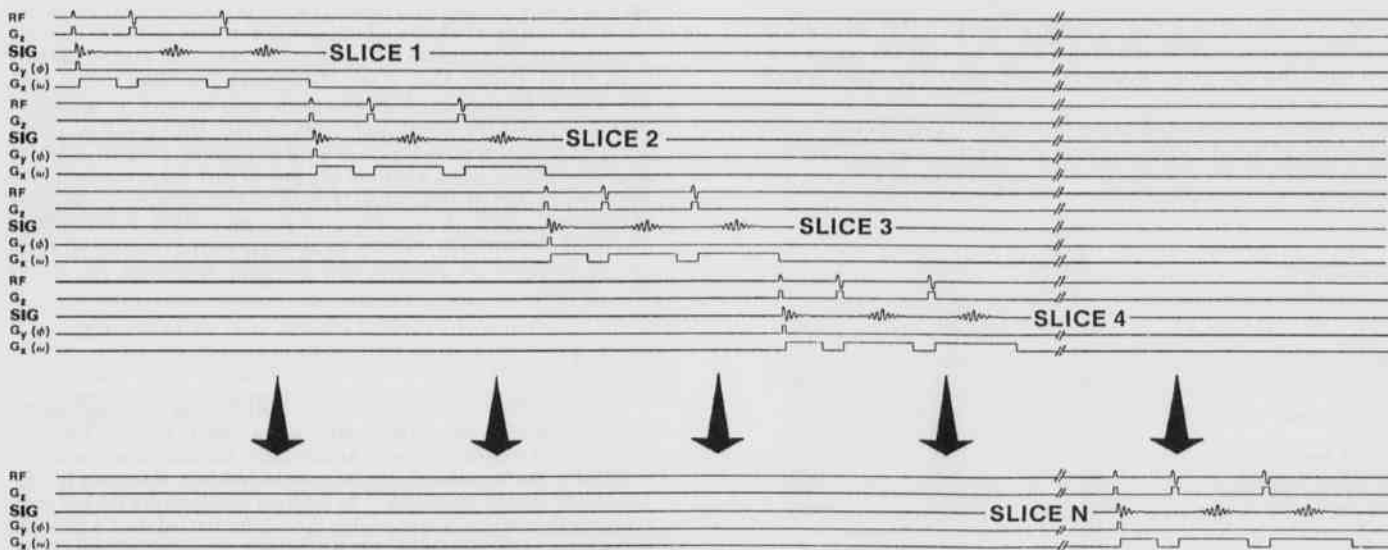

Figure 15. Multislice, Multiecho Spin Echo Imaging.

Principles and Clinical Applications of Magnetic Resonance

THREE DIMENSIONAL FOURIER TRANSFORM

Instead of multislice imaging, true volume imaging can be performed by using three-dimensional Fourier transform (3DFT). The z gradient in this technique is used to encode frequency in the z direction. The phase is encoded separately in the x and y directions by the use of the x and y gradients. The complex frequency distribution that is obtained is decoded by 3DFT and utilized to generate images of slices in any projection. There is an isotropic volume collection if the step size of the z gradient is the same as the x and y gradients; it is anisoptropic otherwise.

IMAGING TIME IN MRI

In order to generate high quality images, one pulse sequence and data collection process for each line are not sufficient for a good image. Therefore, it is necesary to utilize repetitive pulse sequences to collect multiple data sets from a single line and average before image reconstruction. The following equation is used to calculate the imaging time:

$$\text{Time} = N_y \times n \times TR, \tag{13}$$

where N_y = the number of gradient steps in the y or phase-encoding direction, n = the number of signals averaged into one line, and TR = the sequence repetition time.

The time to acquire images is one of the primary problems of MRI. Two to 20 minutes are common imaging times. Again, if we look at equation 13, we see that by reducing TR we can significantly reduce the imaging time. This can be done by using tip angles, which are less than 90°. This would result in nuclei returning to equilibrium in significantly less time, allowing smaller TR's. However, a gradient reversal or gradient echo technique also would have to be used instead of the 180° rephasing pulse.

IN-VIVO MAGNETIC RESONANCE STUDIES

CONTRAST AGENTS

In-vivo NMR images are dependent upon proton density, T_1, T_2, and flow characteristics. Both relaxation times reveal a significant difference between normal and abnormal tissue (see Table 2). A prediction by some earlier workers was that a knowledge of the first three parameters (for a particular tissue) would enable a successful non-invasive tissue biopsy. However, with greater clinical use of MRI, the difficulty in separating lesions, such as neoplasms or abscesses, of the central nervous system from surrounding cerebral edema became apparent. Several

Table 2. Relative Spin Density and Approximate T_1 and T_2 Relaxation Times at a Field Strength of 1.0 Tesla for Various Tissues.

TISSUE	RELATIVE SPIN DENSITY	T_1(ms)	T_2(ms)
Fat	98	180	90
Liver	91	270	50
Renal cortex		360	70
White matter	100	390	90
Spleen	92	480	80
Gray matter	94	520	100
Muscle	100	600	40
Renal medulla		680	140
Blood	90	800	180
Cerebrospinal fluid	96	2000	300
Water		2500	2500
Air	<1		
Lung	1-5		
Cortical bone	1-10		
Kidney	95		
Pancreas	86		

investigators suggested the use of contrast agents as used with CT-scan, to enhance the usefulness of MRI (Bydder et al., 1982; Alfidi et al., 1982). Gadopentetic acid (Gd-DTPA) is the most commonly used contrast agent in MRI. This paramagnetic metal ion chelate enhances proton relaxation, shortening both T_1 and T_2 in-vivo. The definition of renal functional status, improved definition of normal anatomy and pathologic lesions, and improvement in the definition of lesion vascularity are among the benefits of contrast enhancement in MRI (Runge et al., 1983).

LOCALIZED SPECTROSCOPY

In addition to its diagnostic usefulness as a non-invasive in-vivo imaging tool, use of NMR spectroscopy to monitor in-vivo metabolites and physiologically important ions in organs and tissues provides an unparalleled opportunity for new venues in medical research. A combination of in-vivo proton imaging and localized spectroscopy on a particular metal ion (such as ^{23}Na, ^{31}P, or ^{39}K) can give the physiological state of the tissue in the localized region. For example, the ^{31}P spectrum from muscle or brain tissue contains signals from adenosine triphosphate (ATP), inorganic phosphate, creatine phosphate, and sugar phosphates which can be used to calculate the concentrations of each of these components in the tissue. Intracellular pH of the tissue can be calculated from the position of ^{31}P signal from inorganic phosphate (Hoult et al., 1974; Dawson et al., 1977; and Chance et al., 1980). A combination of ^{31}P and ^1H NMR spectroscopy allows the study of the phosphorylated metabolites by ^{31}P NMR and determination of intracellular lactate levels by ^1H NMR (Bekar et al., 1985).

^{13}C MRI

Since the natural abundance of ^{13}C is only 1.1%, only compounds such as triacylglycerols or glycogen, which can have very high intracellular concentrations, are detectable at the natural abundance level by ^{13}C NMR. However, this low natural abundance has been used to advantage for metabolic studies by following the flow of ^{13}C label introduced by specifically labelled substrates (Cohen, 1983; Reo et al., 1984; Shulman et al., 1979). Ackerman and co-workers (Reo et al., 1984) have used this technique by giving ^{13}C enriched glucose intravenously to fasted rats to follow the kinetics of glycogenesis from glucose and subsequent glycogenolysis in-vivo under a number of conditions. This was done by using a surface coil which was placed on a surgically exposed liver. They also studied the effects of hormonal treatment on hepatic glucose metabolism in-vivo by ^{13}C NMR. Natural abundance ^{13}C NMR spectra of human muscle samples, before and after removal of neutral fat by extraction with isopentane, have been used by Baramy et al. (1984). Earlier Alger et al., (1981) ran a feasibility study to obtain natural abundance ^{13}C NMR species coupled with ^1H spectra of muscle in-vivo in the human arm. More recently, Starewicz et al. (1985) acquired natural abundance ^{13}C spectra of a human subject. All spectra were obtained using a surface coil placed over the liver, chest, and the head. No spatial localization techniques were used when obtaining the spectra. Clearly, it is evident that the application of whole body ^{13}C NMR spectroscopy without surgical exposure is dependent upon the development of sensitive and practical techniques for spatial localization.

^{19}F MRI

^{19}F is a relatively attractive nucleus for MRI imaging and spectroscopy since it has a 100% natural abundance and a relative sensitivity of 0.83 (compared to 1.00 for protons). Additionally, minimal adjustments are required in the instrumentation because its resonant frequency is very close to the proton frequency. The inherent problems are the low concentrations at which it is available in-vivo (estimated as 2.6 gms for a 70Kg man) (Thomas et al., 1982). The soft tissue concentration will be much less since most fluorine is incorporated in bone (fluorapetite). The potential for ^{19}F NMR imaging using fluorodeoxyglucose (FDG) has been reviewed by Thomas et al. (1985) who showed that 3-FDG

Rao P. Gullapalli, Teresa T. Evans, and Roger M. Hawk

holds considerable promise for NMR applications in the study of glucose metabolism. Nunnally *et al.* (1985) studied the uptake and metabolism of fluorinated anti-tumor agents such as 5-fluorouracil with ^{19}F spectroscopy in intact rabbits. They postulated the nearly simultaneous observation of ^{19}F and phosphorus metabolism by ^{31}P utilizing a doubly tuned coil which represents a significant application of in-vivo NMR in the evaluation of tumor therapy.

The extremely low endogeneous concentration of mobile fluorine coupled with high NMR sensitivity and 100% natural abundance makes ^{19}F very suitable for use in in-vivo studies which involve the use of biocompatible fluorine tracer compounds.

^{23}Na AND ^{39}K MRI

The cellular compositions of sodium and potassium and their concentration gradients across the cellular membrane play a vital role in various physiological processes. Excess accumulation of sodium ions in the cells is known to be the cause for certain cancers, diabetes, and hypertension (Camerson *et al.*, 1980; Boynton *et al.*, 1982; Moore *et al.*, 1983; Blaustein, 1977). Sodium magnetic resonance has the potential of corrtributing physiological and clinical information which is unavailable from either proton or phosphorus NMR studies. Applications include the study of tumor processes, normal cardiac or renal physiology, and electrophysiological events such as the alterations of the intracellular Na$^+$ and/or Na$^+$/K$^+$ ATPase activity due to pharmacological intervention or pathological events. The recent advent of lanthanide shift reagents has enabled separation of the extracellular sodium signal from that of the intracellular signal (Gupta and Gupta, 1982; Pike *et al.*, 1984). Since the overall sensitivity of ^{23}Na is near that of ^{1}H nucleus, it has been used for generating images (Hilal *et al.*, 1985; Ra *et al.*, 1986; Turski *et al.*, 1987; Burstein and Mattingly, 1989), even though the images do not provide the same quality of anatomic detail obtained with proton NMR.

It was observed by Cope (1965, 1967) that the concentrations of sodium in biological tissue as determined by ^{23}Na NMR was 60% smaller when compared to other chemical techniques. This leads to the famous NMR 'visibility' question. Sodium and potassium are quadrupolar nuclei and they exhibit NMR 'invisibility' since two of the outer transitions for a quadrupolar nucleus, that is, $-3/2 \rightarrow -1/2$ and $1/2 \rightarrow 3/2$, have a different resonance frequency and a very short relaxation time, which broadens the signal obtained at these frequencies. Thus, only the central transition ($-1/2 \rightarrow 1/2$) is observed which comprises 40% of the total signal intensity (Hubbard, 1970; Bull, 1982). We have studied the visibility of ^{7}Li in biological tissue extensively in our laboratory and find that ^{7}Li visibility decreases by 10-15% going from 40 mm ^{7}Li to 1 mm ^{7}Li in red blood cells (Gullapalli *et al.*, 1990).

The use of shift reagents for in-vivo studies is being actively pursued and rat studies which correlated the accumulation of intracellular sodium with the deletion of high energy phosphorus metabolites indicated that the rate of sodium accumulation increased with the depletion of ATP (Blum *et al.*, 1986; Balschi *et al.*, 1986). Except for imaging, no other studies have been done on humans. With the advancements in instrumentation, non-toxic shift reagents, and better spatial localization techniques, ^{23}Na NMR techniques will be applied to study various physiological processes in the very near future.

The major disadvantage of ^{39}K NMR is its poor sensitivity. Some work is being done to study the transport kinetics of ^{39}K by using ^{87}Rb as a sensitive probe (improves the sensitivity by a factor of 19) (Allis *et al.*, 1989). No studies on humans have yet been performed. Research continues in the enhancement of the ^{39}K signal and other new techniques that may eliminate the use of shift reagents which may alter the biological activity.

CONCLUSION

Over the years, the application of MRI imaging and spectroscopy in-vivo has broadened the horizons for different nuclei. This has enabled the scientist to innovate new pulse sequences, improve sensitivity through better instrumentation, and better in-vivo localization techniques. There is always a need to reduce the scan time on a patient for diagnostic purposes. The advances in research have enabled researchers to better understand and characterize flow phenomena, especially blood flow in the vasculature. The emphasis is also in the direction of higher fields for imaging purposes. The current FDA regulations permit the use of up to 1.5 Tesla magnets for in-vivo imaging purposes. Research on small animals is being done at fields as high as 9.0 Tesla. Four Tesla magnets are being used for in-vivo human research at a few locations in the US. Generally, higher fields would enable one to obtain better spectroscopy results rather than just improved images. A combination of imaging and localized spectroscopy (as an indicator for metabolic character of tissue in-vivo) appears to be the direction for magnetic resonance in medicine.

LITERATURE CITED

ABRAGAM, A. 1961. The principles of nuclear magnetism, Chapter VIII, Oxford University Press, London and New York.

ALFIDI, R.J., J.R. HAAGA, S.J. EL YSONEF, P.J. BRYAN, B.D. FLETCHER, J.P. LIPUMA, S.C. MORRISON, B. KAUFMAN, J.B. RICHEY, W.S. HINSHAW, D.M. KRAMER, H.N. YOUNG, A.M. COHEN, H.E. BUTLER, A.E. AMENT, and J.M. LIEBERMAN. 1982. Preliminary experimental results in humans and animals with a super-conducting whole body nmr scanner, Radiology 143:175-181.

ALGER, J.R., L.O. SILLERUD, K.L. BEHAN, R.J. GILLIES, R.G. SHULMAN, R.E. CORDON, D. SHAW, and P.E. HANLEY. 1981. In vivo carbon-13 nuclear magnetic resonance studies of mammals, Science 214:660.

ALLIS, J.L., R.M. DIXON, A.M. TILL, and G.K. RADDA. 1989. ^{87}Rb studies for evaluation of K$^+$ fluxes in human erythrocytes, J. of Mag. Res. 85:524-529.

BALSCHI, J.A., J.A. BITTLE, and J.S. INGWALL. 1986. Ischemia in the intact rat leg by interleaved P-31 and Na-23 nmr wing: a shift reagent to discriminate intra- and extracellular sodium, (abstract), Fifth Annual Meeting of the Society of Mag. Res. in Med. 2:343-344.

BARAMY, M., D.D. DOYLE, G. GRAFF, W.M. WESTLER, and J.L. MARKLEY. 1984. 'Natural abundance ^{13}C nmr spectra of human muscle, normal and diseased, Mag. Res. Med. 1:30.

BEKAR, K.L., J.A. DEN HOLLANDER, O.A.C. PETROFF, H.P. HETHERINGTON, J.W. PRICHARD, and R.G. SHULMAN. 1985. Effect of hypoglycemic encephalopathy upon amino acids, high energy phosphates and pH in the rat brain in vivo: detection by sequential ^{1}H and ^{31}P nmr spectroscopy, J. Neurochem. 44:1045-1055.

BLAUSTEIN, M.P. 1977. Sodium ions, calcium ions, blood pressure regulation, and hypertension: a reassessment and a hypothesis, Am. J. Physiol. 232:c165-175.

BLUM, H., M.D. SCHNALL, G.P. BUZBY, and B. CHANCE. 1986. Sodium flux and high energy phosphate content in ischemic skeletal muscle, (abstract), Fifth Annual Meeting of the Society of Mag. Res. in Med. 2:339.

BOYNTON, A.L., W.L. MCKEEHAN, and J.F. WHITFIELD. 1982. Symposium on ions, cell profileration, and cancer, New York, Academic Press.

BULL, T.E. 1982. Nuclear magnetic relaxation of spin-3/2 nuclei involved in chemical exchange, J. Mag. Res. 8:344-353.

Principles and Clinical Applications of Magnetic Resonance

BURSTEIN, D. and M. MATTINGLY. 1989. Magnetic resonance imaging of intracellular sodium, J. Mag. Res. 83:197-204.

BUSHONG, STEWART C. 1988. Magnetic resonance imaging - physical and biological principles, The C.V. Mosby Company, St. Louis, Washington, D.C., and Toronto.

BYDDER, G.M., R.E. STEINER, I.R. YOUNG. 1982. Clinical nmr imaging of the brain: 140 cases, Am. J. of Roentgenol, 139:215-236.

CAMERSON, I.L., N.K.R. SMITH, T.B. POOL, and R.L. SPARKS. 1980. Intracellular concentration of sodium and other elements as related to mitogens and oncogenesis in vivo, Cancer Research, 40:1493-1500.

CHANCE, B., S. ELEFF, and J.L. LEIGH. 1980. Noninvasive, nondestructive approaches to all bioenergetics, Proc. Natl. Acad. Sci. USA, 77:7430-7434.

COHEN, S.M. 1983. Simultaneous ^{13}C and ^{31}P nmr studies of perfused rat liver: effects of insulin and glucagon and a ^{13}C assay of free Mg^{++}, J. Biol. Chem. 14:294.

COPE, F.W. 1965. Nuclear magnetic resonance evidence for complexing of sodium ions in muscle, Proc. Natl. Acad. Sci. USA, 54:225-227.

COPE, F.W. 1967. NMR evidence for complexing of Na$^+$ in muscle, kidney, and brain, and by actomyosis: the relation of cellular complexing of Na$^+$ to water structure and to transport kinetics, J. Ge. Physiol., 50:1353-1375.

DAWSON, M.J., D.G. GADIAN, and D.R. WILKIE. 1977. Studies of living contracting muscle by ^{31}P nuclear magnetic resonance, R.A. Dwek, I.D. Campbell, R.F. Richards, and R.J.P. Williams (eds.), NMR in Biology, London, Academic Press, 289-321 pp.

EMSLEY, J.W., J. FEENEY, and L.H. SUTCLIFF. 1965. High resolution nmr spectroscopy, Chapter 2, Pergamon Press, Oxford.

FARRAR, T.C. and E.D. BECKER. 1971. Pulse and fourier transform nmr, Academic Press, London and New York.

GULLAPALLI, R.P., R.M. HAWK, and R.A. KOMOROSKI. 1990. A ^{7}Li nmr study of visibility, spin relaxation, and transport in normal human erythrocytes, Magnetic Resonance in Medicine. (In press.)

GUPTA, R.K. and P. GUPTA. 1982. Direct observation of resolved resonances from intra- and extracellular sodium-23 ions in nmr studies of intact cells and tissues using dysprosium(III) tripolyphosphate as paramagnetic shift reagent, J. Mag. Res., 47:344-350.

HAHN, E.L. 1950. Phys. Rev., 80:580.

HAWK, R.M. 1973. A study of ^{207}Pb relaxation using pulsed nuclear magnetic resonance, Dissertation, The University of Michigan.

HILAL, S.K., A.A. MAUDSLEY, J.B. RA et al. 1985. In vivo nmr imaging sodium-23 in the human head, J. Comput. Assist. Tomography, 9:1-7.

HOULT, D.I., S.J.W. BUSBY, D.G. GADIAN, G.K. RADDA, R.E. RICHARDS, and P.J. SEELEY. 1974. Observation of tissue metabolites using ^{31}P nmr, Nature 252:285-287.

HUBBARD, P.S. 1970. Non-exponential nuclear magnetic relaxation by quadrupole interactions, J. Chem. Phys., 53:985-989.

MOORE, R.D., J.W. MUNFORD, and T.J. PILLSWORTH JR. 1983. Effects of streptozotocin diabetes and fasting on intracellular sodium and adenosine triphosphate in rat skeletal muscle, J. Physiol. (Lon.), 338:277-294.

NUNNALLY, R.L., E.E. BABCOCK, and P. ANTICH. 1985. The direct observation of 5-fluorouracil metabolism by the liver in the intact rabbit: a 19-F nmr study, (abstract), The Society of Magn. Res. in Med., Fourth Annual Meeting, London, 810-811 pp.

PAKE, G.E. 1950. Amer. J. Phys., 18:438.

PIKE, M.M., E.T. FOSSEL, T.W. SMITH, and C.S. SPRINGER, JR. 1984. High resolution ^{23}Na nmr studies of human erythrocytes: use of aqueous shift reagents, Am. J. Physiol., 246:C528-C536.

RA, J.B., S.K. HILAL, and Z.H. CHO. 1986. A method for in vivo mr imaging of the short T_2 component of sodium-23, Mag. Res. Med., 3:296-302.

REO, N.V., C.S. EWY, B.A. SIEGFRIED, and J.J.H. ACKERMAN. 1984. High field ^{13}C nmr spectroscopy of tissue in vivo: a double resonance surface coil probe, J. Mag. res., 56:7.

RUNGE, V.M., J.A. CLANTON, C.M. LUKEHERT, C.L. PARTAIN, and A.E. JAMES JR. 1983. Paramagnetic agents for contrast enhanced nmr imaging: a review, Am. J. Roentgenol., 141:1209-1215.

SHULMAN, R.G., T.R. BROWN, K. UGURBIL, S. OGAWA, S.M. COHEN, and J.A. DEN HOLLANDER. 1979. Cellular applications of ^{31}P and ^{13}C nuclear magnetic resonance, Science, 205:160.

SLICHTER, C.P. 1963. Principles of magnetic resonance, Harper, New York.

STAREWICZ, P.M., G. LUND, and S. HOHNSON. 1985. In vivo carbon-13 spectroscopy at 1.4T in a 1mm bore clinical mr imaging system, Radiology, 157:61.

THOMAS, S.R., J.L. ACKERMAN, and J.R. GOBEL. 1982. Nuclear magnetic resonance techniques as developed modestly within a university medical center environment: what can the small system contribute at this point? Mag. Res. Imag., 1:11-21.

TURSKI, P.A., L.W. HOUSTON, W.H. PERMAN, J.K. HALD, D. TURSKI, C.M. STROTHER, and J.F. SACKETT. 1987. Experimental and human brain neoplasms: detection with in vivo sodium mr imaging, Radiology, 163:245-249.